



# Tailored bimetallic synergy of iron–cobalt sulfide anchored to S-doped carbonized wood fiber for high-efficiency oxygen evolution reaction

Bin Zhao, Wanjuan Zeng, Wenxi Zhang, Sha Chen, Han Xu<sup>\*</sup>, Yu Liao, Yuanyuan Liao, Yan Qing<sup>\*</sup>, Yiqiang Wu

College of Materials Science and Engineering, Central South University of Forestry and Technology, Changsha 410004, PR China

## ARTICLE INFO

### Keywords:

Electrocatalyst  
Wood fiber  
Bimetallic synergy  
Oxygen evolution reaction  
Fe<sub>92</sub>Co<sub>08</sub>S

## ABSTRACT

Decoupling the scaling relation of intermediates is an effective strategy to improve the oxygen evolution reaction (OER) catalytic efficiency. Herein, S-doped carbon-confined Fe<sub>92</sub>Co<sub>08</sub>S nanoparticles (Fe<sub>92</sub>Co<sub>08</sub>S@SC) anchored to S-doped carbonized wood fiber (SCWF) are fabricated via simple synchronous carbonization and sulfidation. Due to the synergistic catalytic effect of bimetallic and the unique structural effect of the supported catalyst, Fe<sub>92</sub>Co<sub>08</sub>S@SC/SCWF exhibit excellent OER catalytic efficiency with an overpotential of 238 mV at 50 mA cm and stability up to 100 h. Furthermore, a high current density of 500 mA cm<sup>-2</sup> at an overpotential of 281 mV was achieved. Theoretical calculations and electrochemical characterizations confirm that bimetallic synergies can accelerate the surface reconstruction of Fe<sub>92</sub>Co<sub>08</sub>S@SC with highly efficient OER activity. For zinc–air battery applications, Fe<sub>92</sub>Co<sub>08</sub>S@SC/SCWF exhibits superior power density and stability over commercial RuO<sub>2</sub>. This work provides insights into the preparation of supported electrocatalysts with bimetallic synergy for high-efficiency OER.

## 1. Introduction

Hydrogen (H<sub>2</sub>) energy has outstanding energy density and environmental preservation qualities, and it has thus been regarded as one of the best alternatives to traditional energy sources [1,2]. Electrolysis of water is an effective and ecologically beneficial method for H<sub>2</sub> production. However, a considerable amount of energy is required for the oxygen evolution reaction (OER) at the anode during water splitting to overcome the energy barrier of four-electron transfers. In addition, O–O bond formation is extremely challenging, resulting in a high thermodynamic voltage requirement for the OER (1.23 V vs. RHE) [3,4]. According to the adsorption evolution mechanism, the adsorption force of the oxyradical intermediate can determine the activity of the OER, and the scaling relation can limit the degree of adsorption optimization [5]. In further details, the binding energies of the intermediary molecules \*OH and \*OOH to the active site play a major role in the scaling relation of OER. It is believed that decoupled the scaling relation of intermediates by catalyst electronic structure optimization and surface-interface tuning is the best strategy for producing effective OER [6,7].

To break the scaling relation in OER intermediates, researchers have

proposed strategies, such as doping of high-valence metal ions [8,9], tuning of O–O coupling [10,11], spin polarization [12,13], and \*OOH stabilization [14–16], for obtaining efficient OER electrocatalysts. However, most advanced OER electrocatalysts still rely on the use of expensive precious metals, such as IrO<sub>2</sub> and RuO<sub>2</sub>. Furthermore, these electrocatalysts exhibit poor performance at high current densities (>500 mA cm<sup>-2</sup>), which are required for commercial and industrial applications; this condition further hinders the widespread adoption of electrolyzed water for H<sub>2</sub> production [17,18]. A number of nonnoble metal electrocatalysts, such as Co-, Ni-, and Fe-based materials, have been utilized in the OER [19,20]. However, most of these electrocatalysts consist of a single metal element and usually have a more limited OER catalytic efficiency. Compared with monometallic-based electrocatalysts, bimetallic sulfide-based electrocatalysts have attracted much attention due to their excellent OER activity and stability. The synergistic effect of bimetals can modulate the electronic structure and accelerate the surface reconstruction to generate metal (oxy)hydroxides, thus improving the performance of electrocatalysts [21]. However, several challenges have been associated with bimetallic-based electrocatalysts. The introduction of two metals often necessitates the implementation of additional complex synthesis strategies, and the synergy

<sup>\*</sup> Corresponding authors.

E-mail addresses: [xuh@csuft.edu.cn](mailto:xuh@csuft.edu.cn) (H. Xu), [qingyan@csuft.edu.cn](mailto:qingyan@csuft.edu.cn) (Y. Qing).

<https://doi.org/10.1016/j.apcatb.2024.123947>

Received 12 September 2023; Received in revised form 31 January 2024; Accepted 9 March 2024

Available online 11 March 2024

0926-3373/© 2024 Elsevier B.V. All rights reserved.

between metals may be restricted by factors, such as crystal structure and coordination environment, resulting in limited utilization of bimetallic [22,23]. Metal-organic frameworks (MOFs) are formed by the connection of metal ions and organic ligands. These materials have an adjustable composition, high utilization rate of metal active centers, and heteroatomic functional groups that can be customized with well-defined functions, which are conducive to the construction of bimetallic-based electrocatalysts. In general, direct pyrolysis of MOFs can be used to obtain various carbon-based materials with a controllable morphology. However, traditional MOF-derived carbon-based materials usually exist in powder form and are highly prone to agglomeration, which can hinder the exposure of active sites. Researchers have attempted to introduce substrates, such as graphene and carbon fiber, to MOFs to prepare supported electrocatalysts to expose more active sites and improve conductivity [24]. However, substrate preparation often involves the use of hazardous chemicals that are nonenvironmentally friendly. Moreover, the coupling of the hybrid interface between substrates and MOFs requires precise control, and the synthesis methods tend to be intricate [25]. In addition, stability may be substantially compromised during operations under high potential or strong acidic/alkaline conditions [26]. Therefore, the preparation of MOF-derived supported electrocatalysts should involve the introduction of environmentally friendly, practical, and stable substrates.

Wood fiber (WF), characterized as a renewable biomass material, stands out for its abundant surface-active functional groups, thereby presenting a potential platform for nucleation sites conducive to the integration of exogenous heterogeneous functional components. Following carbonization, WF undergoes a transition into high-strength carbonaceous materials boasting exceptional electrical conductivity [27–29]. The outlined features accentuate the research and exploratory potential of WF as a substitute for conventional carbon materials. Herein, a supported electrocatalyst constructed using MOF-74-FeCo-derived  $\text{Fe}_{0.92}\text{Co}_{0.08}\text{S}$  nanoparticles with bimetallic embedded in a rugby ball-like S-doped carbon matrix and direct growth on S-doped carbonized WF (SCWF) was fabricated for OER via a simple synchronous carbonization and sulfidation process. Benefiting from the unique structural effect of the supported catalyst,  $\text{Fe}_{0.92}\text{Co}_{0.08}\text{S@SC/SCWF}$  avoids the agglomeration problem commonly seen in MOFs derived carbon composites, and can provide a larger specific surface area and better electrical conductivity. And then, the synergistic catalysis of the bimetallic in  $\text{Fe}_{0.92}\text{Co}_{0.08}\text{S@SC}$  can result in excellent catalytic efficiency for OER. The  $\text{Fe}_{0.92}\text{Co}_{0.08}\text{S@SC/SCWF}$  achieved a current density of  $50 \text{ mA cm}^{-2}$  at an overpotential of 238 mV during catalyzation by OER. Moreover, a 0.14% attenuation of activity was observed after 100 h at  $50 \text{ mA cm}^{-2}$ . Notably, a high current density of  $500 \text{ mA cm}^{-2}$  was achieved at an overpotential of 281 mV. Density functional theory calculations and electrochemical characterizations confirmed the synergistic catalytic effect of the bimetal in  $\text{Fe}_{0.92}\text{Co}_{0.08}\text{S@SC}$ , where the introduction of Co led to a higher electron density for Fe, which accelerated the surface reconstruction of  $\text{Fe}_{0.92}\text{Co}_{0.08}\text{S@SC}$  to generate the active  $\text{FeCoOOH}$  phase, and thus improved the OER activity. In zinc-air battery (ZAB) application,  $\text{Fe}_{0.92}\text{Co}_{0.08}\text{S@SC/SCWF}$  as cathode attained a higher power density ( $177.86 \text{ mW cm}^{-2}$ ) and better cycle stability (negligible attenuation at 100 h) than commercial  $\text{RuO}_2$ .

## 2. Experimental section

### 2.1. Synthesis of MOF-74-FeCo/WF

$\text{FeCl}_2 \cdot 4 \text{ H}_2\text{O}$  (0.60 g) and  $\text{Co}(\text{NO}_3)_2 \cdot 6 \text{ H}_2\text{O}$  (0.87 g) were dissolved in 100 mL deionized water, and 0.10 g native poplar fiber was added and macerated for 24 h at room temperature. 2, 5-dihydroxyterephthalic acid (DOBDC, 40.00 mg),  $\text{FeCl}_2 \cdot 4 \text{ H}_2\text{O}$  (39.75 mg), and  $\text{Co}(\text{NO}_3)_2 \cdot 6 \text{ H}_2\text{O}$  (29.10 mg) were dissolved in a mixed solvent of dimethylformamide (10.0 mL), ethanol (2.0 mL), and deionized water (1.0 mL). Then, the

impregnated fiber was added to the above mixed solution, which was then transferred to a Teflon-lined stainless-steel autoclave, kept at  $120^\circ\text{C}$  for 24 h, cooled to room temperature, washed five times with absolute ethanol, and vacuum dried overnight at  $60^\circ\text{C}$  to obtain MOF-74-FeCo/WF.

### 2.2. Synthesis of $\text{Fe}_{0.92}\text{Co}_{0.08}\text{S@SC/SCWF}$ , $\text{FeS@SC/SCWF}$ , $\text{Co}_9\text{S}_8\text{@SC/SCWF}$

In a typical synthesis, 0.3 g of MOF-74-FeCo/WF and 1.0 g of sulfur powders, each loaded into alumina boats, were placed at the center and in the upstream side of the tube furnace, respectively. The tube furnace was first heated from room temperature to  $300^\circ\text{C}$  with a heating rate of  $2^\circ\text{C min}^{-1}$ , and the temperature was maintained at  $300^\circ\text{C}$  for 2 h. Then the temperature was further increased to  $500^\circ\text{C}$  and was kept for 2 h, and finally maintained at  $700^\circ\text{C}$  for 4 h under nitrogen atmosphere. The  $\text{Fe}_{0.92}\text{Co}_{0.08}\text{S@SC/SCWF}$  were obtained after cooling to ambient temperature.  $\text{Co}_9\text{S}_8\text{@SC/SCWF}$  and  $\text{FeS@SC/SCWF}$  use the same preparation process as  $\text{Fe}_{0.92}\text{Co}_{0.08}\text{S@SC/SCWF}$ , except that only a single metal is added in the synthetic process of MOF-74.

### 2.3. Synthesis of SCWF, $\text{Fe}_{0.92}\text{Co}_{0.08}\text{S@SC}$ and $\text{Fe}_{0.92}\text{Co}_{0.08}\text{S@SC/CC}$

SCWF was prepared through direct synchronous carbonization and sulfidation of the WF. The steps of synchronous carbonization and sulfidation are the same as those used for  $\text{Fe}_{0.92}\text{Co}_{0.08}\text{S@SC/SCWF}$ . WF was removed from the prepared  $\text{Fe}_{0.92}\text{Co}_{0.08}\text{S@SC/SCWF}$ , and the synchronous carbonization and sulfidation were unchanged when obtaining  $\text{Fe}_{0.92}\text{Co}_{0.08}\text{S@SC}$ .

The preparation process of  $\text{Fe}_{0.92}\text{Co}_{0.08}\text{S@SC/CC}$  was basically the same as that of  $\text{Fe}_{0.92}\text{Co}_{0.08}\text{S@SC/SCWF}$ , except that the WF was replaced with carbon cloth.

## 3. Results and discussion

### 3.1. Materials characterization

Considering the characteristics of WF, a scheme for the preparation of OER electrocatalysts based on WF was proposed (Fig. 1). WF was added to a solution of ferrous chloride and cobalt nitrate to adsorb  $\text{Co}^{2+}$  and  $\text{Fe}^{2+}$  at room temperature. Fig. S1 shows the Fourier transform infrared spectroscopy spectra of natural WF and WF that adsorbed metal ions. The vibration at the stretching vibration peak showed no change after the adsorption of metal ions; however, the tensile vibration strength decreased considerably, indicating that  $-\text{OH}$  on the surface of WF adsorbed metal ions [30]. Fig. S2 displays X-ray diffraction (XRD) and scanning electron microscopy (SEM) images of natural WF. For natural WF, the diameter ranges between 10 and  $30 \mu\text{m}$ , and peaks at  $2\theta = 14.2^\circ$ ,  $22.5^\circ$  are associated with the crystal faces of (101) and (002) in cellulosic cellulose, respectively [31]. The pre-adsorption of  $\text{Co}^{2+}$  and  $\text{Fe}^{2+}$  allowed the growing MOF-74 particles to anchor to WF (denoted as MOF-74-FeCo/WF). The characteristic peaks in the XRD pattern of MOF-74-FeCo/WF (Fig. S3) were the same as those in the XRD pattern of conventional MOF-74 (CCDC No.1971315). The MOF-74-FeCo/WF precursor was annealed at  $700^\circ\text{C}$  under  $\text{N}_2$  atmosphere, and the desired composite electrocatalyst was obtained through synchronous carbonization and sulfurization. During the thermal decomposition of the MOF-74-FeCo/WF precursor at  $700^\circ\text{C}$  in  $\text{N}_2$  atmosphere and in the presence of sublimated sulfur, WF converted the cooperated  $\text{Co}^{2+}$  and  $\text{Fe}^{2+}$  in MOF-74 to metallic Co and metallic Fe, which reacted with S vapor to form  $\text{Fe}_{0.92}\text{Co}_{0.08}\text{S}$ , which were then uniformly encapsulated within the S-doped carbon matrix. In summary, the MOF-derived supported electrocatalysts ( $\text{Fe}_{0.92}\text{Co}_{0.08}\text{S@SC/SCWF}$ ) with unique structural effects and dual active sites were successfully synthesized via the above process.

Systematic investigation of the structure and composition of

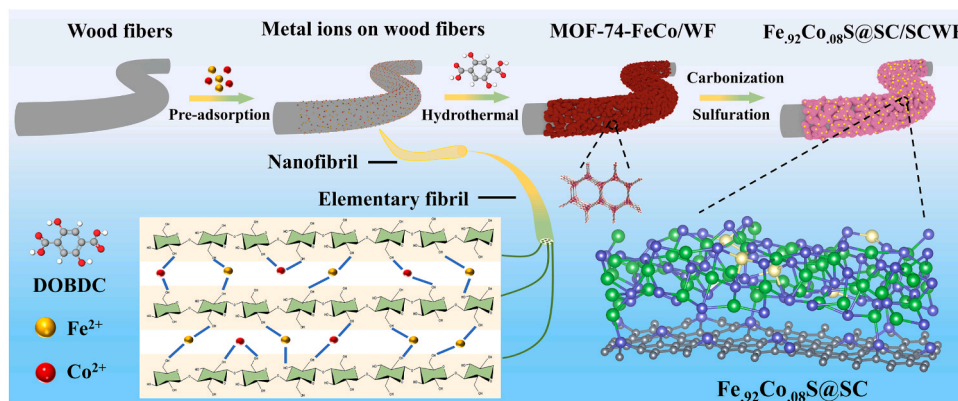


Fig. 1. Schematic of the synthetic process of  $\text{Fe}_{92}\text{Co}_{08}\text{S@SC/SCWF}$ .

composite electrocatalysts was conducted. First, the morphologies of MOF-74-FeCo/WF and  $\text{Fe}_{92}\text{Co}_{08}\text{S@SC/SCWF}$  were characterized and analyzed via SEM. The surface of the WF matrix was uniformly loaded with rugby ball-like particles with sizes ranging from 500 nm to 1.0  $\mu\text{m}$  (Figs. 2a and b). After simultaneous carbonization and sulfidation, the rugby ball-like structure of the prepared  $\text{Fe}_{92}\text{Co}_{08}\text{S@SC/SCWF}$  showed no damage compared with the precursor, and the microparticle surface roughened, further increasing the specific surface area. Fig. S4 shows the corresponding SEM images of  $\text{FeS@SC/SCWF}$ ,  $\text{Co}_9\text{S}_8\text{@SC/SCWF}$ , and  $\text{Fe}_{92}\text{Co}_{08}\text{S@SC}$ . The precise structural information on electrocatalysts was obtained through transmission electron microscopy (TEM) and high-resolution TEM (HRTEM). Fig. 2c displays the particles with a rugby ball-like structure, and Fig. 2d shows the numerous dense pores distributed on its surface. These irregular pores can speed up the flow of

the electrolyte and increase the number of reactional active sites [32]. Figs. S5a and S5b show that nanoparticles with uniform sizes were wrapped in the S-doped carbon layer. The inner encapsulated nanoparticles in the S-doped carbon matrix had a lattice spacing of 0.298 nm, which corresponded to the (110) plane of  $\text{Fe}_{92}\text{Co}_{08}\text{S}$  (Fig. 2e). The selected area electron diffraction (SAED) pattern presented spot and ring structures, which reflects the polycrystalline structure of  $\text{Fe}_{92}\text{Co}_{08}\text{S@SC}$ . Meanwhile, high-angle annular dark-field scanning TEM (HAADF-STEM) and associated energy dispersive spectroscopy elemental mapping (Figs. 2f–j) images showed the uniform distribution of C, S, Fe, and Co within the rugby ball-like microparticles.

XRD was used to examine the crystal structure of the as-synthesized electrocatalysts. Fig. 3a shows the XRD patterns of the three synthesized electrocatalysts, and Fig. S6 displays the XRD patterns of SCWF,

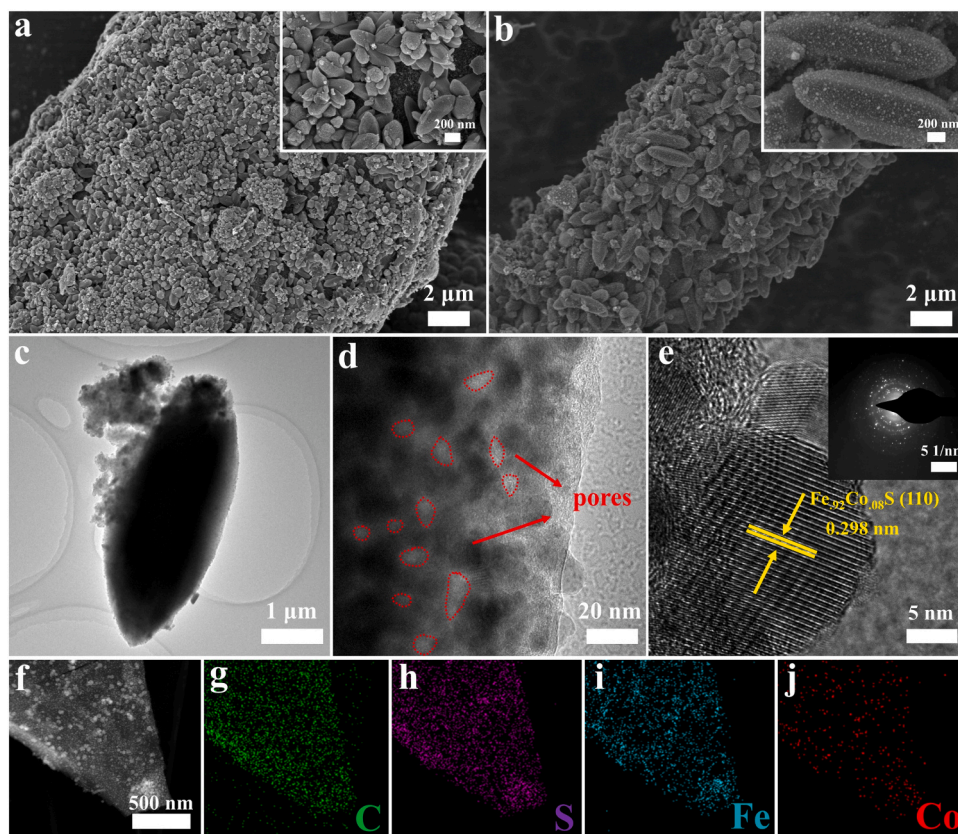
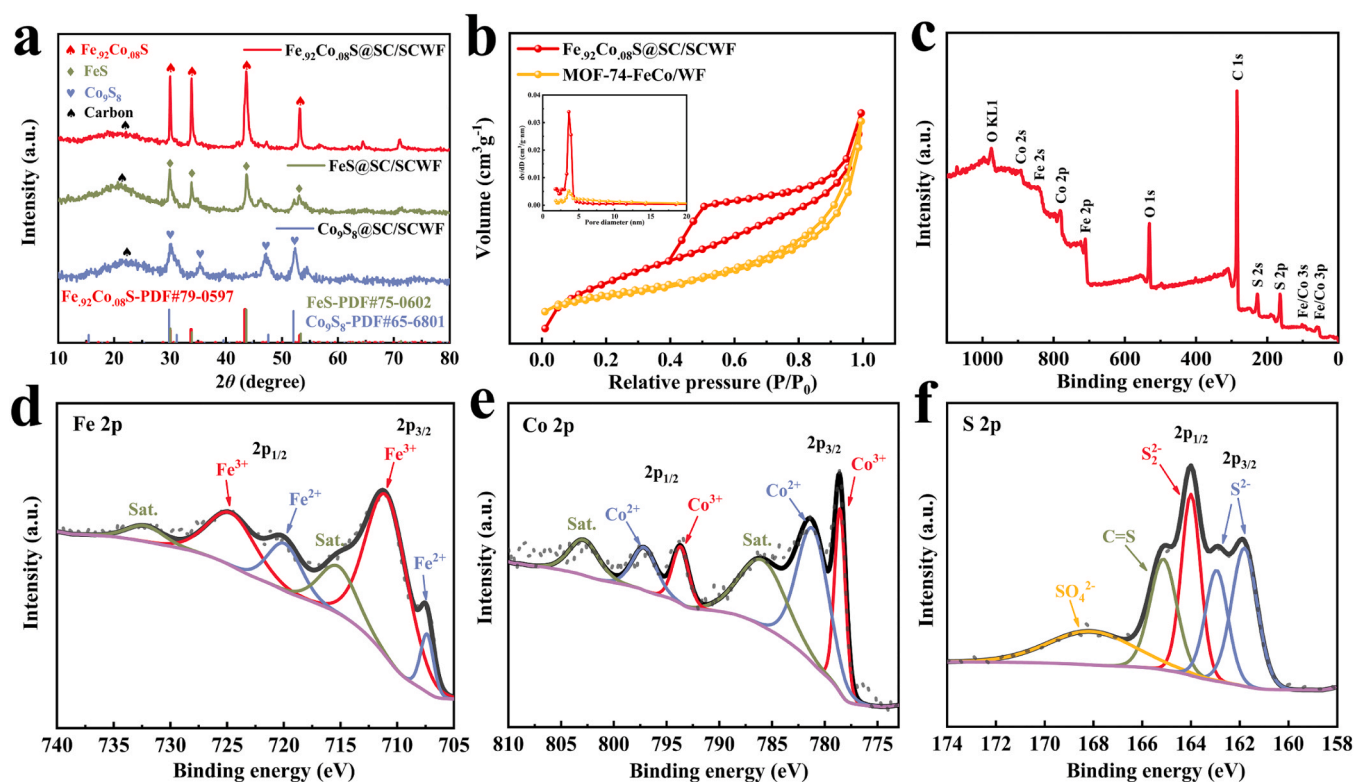


Fig. 2. SEM images of (a) MOF-74-FeCo/WF and (b)  $\text{Fe}_{92}\text{Co}_{08}\text{S@SC/SCWF}$  at different magnifications, (c–d) TEM images of  $\text{Fe}_{92}\text{Co}_{08}\text{S@SC}$ , (e) HRTEM image of  $\text{Fe}_{92}\text{Co}_{08}\text{S@SC}$  (the inset is the corresponding SAED pattern); (f–j) HAADF-STEM image and corresponding elemental mappings of  $\text{Fe}_{92}\text{Co}_{08}\text{S@SC}$ .





**Fig. 3.** (a) XRD patterns of Fe<sub>92</sub>Co<sub>08</sub>S@SC/SCWF, FeS@SC/SCWF, and Co<sub>9</sub>S<sub>8</sub>@SC/SCWF; (b) N<sub>2</sub> adsorption-desorption isothermal curves (the inset is the corresponding pore-size distribution plot) for Fe<sub>92</sub>Co<sub>08</sub>S@SC/SCWF and MOF-74-FeCo/WF; (c) XPS survey spectrum of Fe<sub>92</sub>Co<sub>08</sub>S@SC/SCWF. High-resolution XPS spectra of (d) Fe 2p, (e) Co 2p, and (f) S 2p for Fe<sub>92</sub>Co<sub>08</sub>S@SC/SCWF.

Fe<sub>92</sub>Co<sub>08</sub>S@SC and Fe<sub>92</sub>Co<sub>08</sub>S@SC/CC. The diffraction peaks of Fe<sub>92</sub>Co<sub>08</sub>S@SC/SCWF located at 29.9°, 33.7°, 43.4°, and 53.2° corresponded to the (110), (112), (114), and (300) planes of Fe<sub>92</sub>Co<sub>08</sub>S (PDF#79-0597), respectively. Moreover, the actual molar ratio of Fe and Co in Fe<sub>92</sub>Co<sub>08</sub>S@SC/SCWF was quantitatively confirmed to be 11.2: 1 as measured by ICP-OES (Table S1), which is close to the theoretical value of Fe: Co in Fe<sub>92</sub>Co<sub>08</sub>S. The above results indicate that the successful synthesis of Fe<sub>92</sub>Co<sub>08</sub>S in Fe<sub>92</sub>Co<sub>08</sub>S@SC/SCWF via simultaneous carbonization and sulfidation procedure. In addition, the XRD patterns of FeS@SC/SCWF and Co<sub>9</sub>S<sub>8</sub>@SC/SCWF were consistent with those of FeS (PDF#75-0602) and Co<sub>9</sub>S<sub>8</sub> (PDF#75-2023), respectively. N<sub>2</sub> adsorption-desorption tests were performed on Fe<sub>92</sub>Co<sub>08</sub>S@SC/SCWF to determine their pore structure and pore size distribution. Fe<sub>92</sub>Co<sub>08</sub>S@SC/SCWF showed evident hysterescence rings, corresponding to type-IV isotherms and indicating that it contained many mesoporous structures (pore size: approximately 3.8 nm, Fig. 3b). The calculated Brunauer-Emmett-Teller surface area and pore volume of Fe<sub>92</sub>Co<sub>08</sub>S@SC/SCWF were around 208.7 m<sup>2</sup>g<sup>-1</sup> and 0.13 cm<sup>3</sup>g<sup>-1</sup>, respectively, which are higher than those of MOF-74-FeCo/WF (22.5 m<sup>2</sup>g<sup>-1</sup> and 0.05 cm<sup>3</sup>g<sup>-1</sup>).

X-Ray photoelectron spectroscopy (XPS) was used to determine the surficial composition and valence of Fe<sub>92</sub>Co<sub>08</sub>S@SC/SCWF. Fig. 3c depicts the survey XPS spectrum of Fe<sub>92</sub>Co<sub>08</sub>S@SC/SCWF, except for a certain amount of O that may contribute to the partial surface oxidation of Fe<sub>92</sub>Co<sub>08</sub>S@SC/SCWF. Only Fe, Co, S, and C were discovered. In the high-resolution Fe 2p XPS spectrum of Fe<sub>92</sub>Co<sub>08</sub>S@SC/SCWF (Fig. 3d), the peaks at 707.3 and 720.0 eV were attributed to 2p<sub>3/2</sub> and 2p<sub>1/2</sub> of Fe<sup>2+</sup>, respectively; the peak at 710.9 eV was attributed to 2p<sub>3/2</sub>, and that at 724.6 eV was due to 2p<sub>1/2</sub> of Fe<sup>3+</sup> [33]. The high-resolution XPS spectrum of Co 2p of Fe<sub>92</sub>Co<sub>08</sub>S@SC/SCWF (Fig. 3e) can be broken down into four primary peaks: those of Co 2p<sub>1/2</sub> at 797.2 and 793.3 eV and those of Co 2p<sub>3/2</sub> at 780.9 and 778.5 eV. The peaks at 780.9 and 797.22 eV indicated the presence of Co<sup>2+</sup>, and those at 778.5 and

793.3 eV implied the presence of Co<sup>3+</sup> [34]. The peaks at 161.8 and 162.9 eV were ascribed to S 2p<sub>3/2</sub> and S 2p<sub>1/2</sub>, respectively, matching the metal-sulfur bond of Fe<sub>92</sub>Co<sub>08</sub>S@SC/SCWF in the high-resolution S 2p spectrum (Fig. 3f) [35]. The characteristic peak at 165.1 eV was attributed to the C=S bond. The distinctive peak at 168.2 eV was linked to the sulfate component (SO<sub>4</sub><sup>2-</sup>), probably because of the surface oxidation of sulfur species in air [36,37]. The XPS spectrum (Fig. S7) of C 1s revealed characteristic peaks at 284.8, 285.8, and 288.1 eV, which were attributed to C=C, C-S, and O-C=O, respectively, indicating the successful synthesis of the S-doped carbon matrix. The O-C=O bonds implied the existence of O-containing groups in the carbon matrix, endowing the surface with a high hydrophilicity; such conditions provided an intermediate OH<sup>-</sup> adsorption capacity and thus increased the OER activity [38,39]. Furthermore, to verify whether S was doped into the carbon matrix, we collected the XPS spectra of Fe<sub>92</sub>Co<sub>08</sub>S@SC and SCWF. The XPS spectrum of S 2p for Fe<sub>92</sub>Co<sub>08</sub>S@SC and SCWF revealed the presence of C=S bonds (Fig. S8), and the distinctive peak of the C-S bond can also be observed in C 1s. The above results confirm the successful doping of S into the carbon matrix and carbonized WFs. Doping S into the carbon skeleton can change the electronic structure and surface polarity of carbon, which improves its catalytic activity [40,41]. To reveal the electronic interactions between bimetallic, we compared the XPS spectra of Fe<sub>92</sub>Co<sub>08</sub>S@SC/SCWF, FeS@SC/SCWF, and Co<sub>9</sub>S<sub>8</sub>@SC/SCWF (Fig. S9). The Fe 2p binding energy of Fe<sub>92</sub>Co<sub>08</sub>S@SC/SCWF was approximately 0.23 eV lower than that of FeS@SC/SCWF, and the Co 2p binding energy of Fe<sub>92</sub>Co<sub>08</sub>S@SC/SCWF was around 0.38 eV higher than that of Co<sub>9</sub>S<sub>8</sub>@SC/SCWF, which was attributed to the electronic coupling effects between neighboring Fe and Co atoms. This finding proves the synergistic effect between Fe and Co that occurred during the formation of Fe<sub>92</sub>Co<sub>08</sub>S@SC [42-44].





that  $\text{Fe}_{0.92}\text{Co}_{0.08}\text{S@SC/SCWF}$  had a charge transfer resistance of  $0.35\ \Omega$ , further confirming its excellent OER charge transfer kinetics (Fig. 4c shows the equivalent circuit diagram, and Table S2 provides the corresponding fitting data). To gain in-depth information about the reaction kinetics for OER, in situ EIS tests were performed to detect the potential controlling factors of Co introduction on  $\text{Fe}_{0.92}\text{Co}_{0.08}\text{S@SC/SCWF}$ . In situ EIS tests were performed on  $\text{Fe}_{0.92}\text{Co}_{0.08}\text{S@SC/SCWF}$  and  $\text{FeS@SC/SCWF}$ , and the Bode plot results showed (Fig. 4d) that the phase angles in the high and low frequency regions of  $\text{Fe}_{0.92}\text{Co}_{0.08}\text{S@SC/SCWF}$  decreased significantly at applied voltages higher than  $1.468\ \text{V}$ , which represented extremely fast electrocatalytic oxidation reactions; while  $\text{FeS@SC/SCWF}$  showed a faster electrocatalyst oxidation reaction only at  $1.518\ \text{V}$ , indicating that the introduction of Co can accelerate the OER reaction kinetics of  $\text{Fe}_{0.92}\text{Co}_{0.08}\text{S@SC/SCWF}$ .

To further investigate the intrinsic catalytic activity of different electrocatalysts, we investigated the electrochemical surface area (ECSA). ECSA, which is proportional to the electrochemical bilayer capacitance ( $C_{dl}$ ), is an important criterion for quantifying the number of exposed active sites (Fig. 4e and S12) [45].  $\text{Fe}_{0.92}\text{Co}_{0.08}\text{S@SC/SCWF}$  attained a higher  $C_{dl}$  ( $7.18\ \text{mF cm}^{-2}$ ) than  $\text{FeS@SC/SCWF}$  ( $4.09\ \text{mF cm}^{-2}$ ) and  $\text{Co}_9\text{S}_8\text{@SC/SCWF}$  ( $3.47\ \text{mF cm}^{-2}$ ). Based on the  $C_{dl}$  test, the ECSA of  $\text{Fe}_{0.92}\text{Co}_{0.08}\text{S@SC/SCWF}$  ( $179.5\ \text{cm}^2$ ) was higher than those of  $\text{Co}_9\text{S}_8\text{@SC/SCWF}$  ( $102.25\ \text{cm}^2$ ) and  $\text{FeS@SC/SCWF}$  ( $86.75\ \text{cm}^2$ ). The larger ECSA of  $\text{Fe}_{0.92}\text{Co}_{0.08}\text{S@SC/SCWF}$  can be attributed to the encapsulation of  $\text{Fe}_{0.92}\text{Co}_{0.08}\text{S}$  in the S-doped carbon matrix and the synergistic effect of the dual active sites in  $\text{Fe}_{0.92}\text{Co}_{0.08}\text{S@SC}$  microparticles. Theoretically, the ECSA-normalized current density can be used for reliable evaluation of the intrinsic activity of electrocatalysts [46]. Notably,  $\text{Fe}_{0.92}\text{Co}_{0.08}\text{S@SC/SCWF}$  required a minimum overpotential of  $273\ \text{mV}$  to achieve a normalized current density of  $1\ \text{mA cm}^{-2}$  (Fig. S13), which confirmed its considerably intrinsic catalytic activity. This result implies that the excellent OER catalytic efficiency of  $\text{Fe}_{0.92}\text{Co}_{0.08}\text{S@SC/SCWF}$  is due to the synergistic effect of Fe and Co as well as the unique structural effects.

The stability of electrocatalysts is another important index to be considered in their practical applications. Fig. 4f shows the chronopotentiometry response of  $50\ \text{mA cm}^{-2}$  in  $1.0\ \text{M KOH}$  solution for  $\text{Fe}_{0.92}\text{Co}_{0.08}\text{S@SC/SCWF}$ . After continuous operation for  $100\ \text{h}$ , the potential increase was negligible ( $0.14\%$ ), indicating the excellent stability of  $\text{Fe}_{0.92}\text{Co}_{0.08}\text{S@SC/SCWF}$  against OER in alkaline media. For  $\text{FeS@SC/SCWF}$  ( $1.75\%$ ) and  $\text{Co}_9\text{S}_8\text{@SC/SCWF}$  ( $4.05\%$ ), the increases in potential were notably larger than those of  $\text{Fe}_{0.92}\text{Co}_{0.08}\text{S@SC/SCWF}$ , which means that the bimetallic synergies may be beneficial in improving the stability of the catalyst. In addition, when a current density of  $100\ \text{mA cm}^{-2}$  was applied to  $\text{Fe}_{0.92}\text{Co}_{0.08}\text{S@SC/SCWF}$ , the potential of  $\text{Fe}_{0.92}\text{Co}_{0.08}\text{S@SC/SCWF}$  increased by  $1.01\%$  after  $100\ \text{h}$  of operation. More prominently, the potential of  $\text{Fe}_{0.92}\text{Co}_{0.08}\text{S@SC/SCWF}$  showed a  $1.02\%$  increase after the stability test at a high current density of  $500\ \text{mA cm}^{-2}$  for  $100\ \text{h}$  (Fig. S14). This finding proves that  $\text{Fe}_{0.92}\text{Co}_{0.08}\text{S@SC/SCWF}$  also attained excellent electrocatalytic stability at a high current density in the OER process. In addition, the electrocatalytic performance of  $\text{Fe}_{0.92}\text{Co}_{0.08}\text{S@SC/SCWF}$  exceeded that of the reported advanced OER electrocatalysts (Fig. 4g and Table S3). Furthermore, the structure and composition of  $\text{Fe}_{0.92}\text{Co}_{0.08}\text{S@SC/SCWF}$  after the OER stability test were analyzed via SEM, XRD, and XPS. After  $100\ \text{h}$  of stability testing (at  $50\ \text{mA cm}^{-2}$ ), the main components and rugby ball-like structure of  $\text{Fe}_{0.92}\text{Co}_{0.08}\text{S@SC/SCWF}$  exhibited no considerable change (Fig. S15), confirming the excellent structural stability of  $\text{Fe}_{0.92}\text{Co}_{0.08}\text{S@SC/SCWF}$ . Fig. S16 displays the high-resolution XPS spectrum of  $\text{Fe}_{0.92}\text{Co}_{0.08}\text{S@SC/SCWF}$  after the OER stability test. The peaks of Fe 2p and Co 2p shifted positively after OER activity, implying the formation of trivalent cations (Figs. S16a and S16b). The proportion of all trivalent cations increased substantially, consistent with hydroxide formation [47]. The XPS spectrum of S 2p (Fig. S16c) showed a remarkable reduction in peak intensity compared with that before OER activation, indicating the conversion of sulfide to (oxy)hydroxide. It is worth noting that most of the remaining

sulfides exist in the high valence state, namely the sulfate component ( $\text{SO}_4^{2-}$ ). The co-existence of (oxy)hydroxide with  $\text{SO}_4^{2-}$  enhances the electrocatalytic OER activity [48]. Similarly, the XPS spectrum of O 1s after OER activity changed to a great extent (Fig. S16d). The peak value of M–O increased remarkably compared with that before the OER activity, and a new peak appeared at  $531.1\ \text{eV}$ , which was attributed to hydroxide ( $\text{OH}^-$ ). The HRTEM image of  $\text{Fe}_{0.92}\text{Co}_{0.08}\text{S@SC/SCWF}$  after OER stabilization (Fig. S17) can also be observed that an oxide layer is generated on the surface of  $\text{Fe}_{0.92}\text{Co}_{0.08}\text{S@SC}$ . Raman spectrum of  $\text{Fe}_{0.92}\text{Co}_{0.08}\text{S@SC/SCWF}$  were also collected before and after the OER reaction (Fig. S18). A characteristic peak near  $225\ \text{cm}^{-1}$  was present before and after the OER reaction, which could be attributed to  $\text{Fe}_{0.92}\text{Co}_{0.08}\text{S}$  [49]. The broad peaks at  $419$  and  $629\ \text{cm}^{-1}$  in the Raman spectra after OER could be attributed to  $\text{CoOOH}$  and  $\text{FeOOH}$ , respectively, and the two characteristic peaks centered at  $834$  and  $876\ \text{cm}^{-1}$  belong to  $\text{SO}_4^{2-}$  [50,51]. These results confirm the formation of metal (oxy)hydroxides via surface reconfiguration during the OER process.

### 3.3. Unveiling the catalytic mechanism of $\text{Fe}_{0.92}\text{Co}_{0.08}\text{S@SC/SCWF}$ for OER

DFT was used to elucidate the mechanism underlying the superior OER performance of  $\text{Fe}_{0.92}\text{Co}_{0.08}\text{S@SC/SCWF}$  and the synergistic effect of the Fe and Co bimetallic. Structural models of  $\text{Fe}_{0.92}\text{Co}_{0.08}\text{S@SC}$ ,  $\text{FeS@SC}$ , and  $\text{Co}_9\text{S}_8\text{@SC}$  were constructed (Fig. S19). The density of states (DOS) map in Fig. S20 shows that  $\text{Fe}_{0.92}\text{Co}_{0.08}\text{S@SC}$ ,  $\text{FeS@SC}$ , and  $\text{Co}_9\text{S}_8\text{@SC}$  were all continuous at the Fermi energy level, indicating that they all had excellent electrical conductivities. Moreover, the Fermi-level DOS strength indicated that  $\text{Fe}_{0.92}\text{Co}_{0.08}\text{S@SC}$  possessed better conductivity than the single metal system, consistent with the EIS results [52]. Fig. 5a shows that the PDOS intensity of Fe is significantly larger than that of Co in  $\text{Fe}_{0.92}\text{Co}_{0.08}\text{S@SC}$ . The charge density difference of  $\text{Fe}_{0.92}\text{Co}_{0.08}\text{S@SC}$  and  $\text{FeS@SC}$  (Fig. 5b) also prove that there is a strong electronic interaction between Fe and Co, and the electronic interactions brought about by the introduction of Co increase the electron density of Fe, which favors the  $\text{Fe}_{0.92}\text{Co}_{0.08}\text{S@SC}$  surface reconstruction to generate  $\text{FeCoOOH}$ . Based on previous studies, metal sulfides act only as precatalysts at the OER, and the metal (oxy)hydroxides generated by their surface reconstruction are the real active phase [53,54]. Therefore, DFT calculations were performed with the model of  $\text{FeCoOOH}$  and  $\text{FeOOH}$  (Fig. S21). To determine the true active site, the  $\text{OH}^*$  adsorption energies of Fe and Co sites in  $\text{FeCoOOH}$  were calculated (Fig. 5c), and it was found that Fe site in  $\text{FeCoOOH}$  has the most negative  $\text{OH}^*$  adsorption energy ( $-2.07\ \text{eV}$ ), which implies that  $\text{OH}^*$  preferentially adsorbs on the Fe site in  $\text{FeCoOOH}$ , proving it to be the true OER active site [55]. Subsequently, the Gibbs free energies ( $\Delta G$ ) of the intermediates were calculated for each basic step of  $\text{FeCoOOH}$  and  $\text{FeOOH}$  (Figs. S22 and S23). As can be seen from the free energy ladder plots in Fig. 5d, the rate-determining step (RDS) of  $\text{FeCoOOH}$  requires less energy barrier ( $1.60\ \text{eV} < 3.85\ \text{eV}$ ) compared to  $\text{FeOOH}$ . Meanwhile, the d-band centers calculated from the PDOS of Fe in  $\text{FeCoOOH}$  and  $\text{FeOOH}$  are closer to the Fermi energy level compared to those in  $\text{FeOOH}$  (Fig. 5e), which proves that the introduction of Co can change the electronic structure of Fe, thus favoring the adsorption of the reaction intermediates [56]. Therefore, it can be inferred from the results of DFT calculations that the electronic interactions brought about by the introduction of Co into  $\text{Fe}_{0.92}\text{Co}_{0.08}\text{S@SC}$  can increase the electron density of Fe and accelerate the surface reconstruction of  $\text{Fe}_{0.92}\text{Co}_{0.08}\text{S@SC}$ , resulting in the generation of  $\text{FeCoOOH}$  with highly efficient OER activity (Fig. 5f).

### 3.4. Performance of the $\text{Fe}_{0.92}\text{Co}_{0.08}\text{S@SC/SCWF}$ -loaded Zinc-air battery

ZAB has the advantages of being safe, clean, and decarbonized energy storage and has attracted increasing research attention [57]. Given the excellent OER performance of  $\text{Fe}_{0.92}\text{Co}_{0.08}\text{S@SC/SCWF}$ , we assembled a  $\text{Fe}_{0.92}\text{Co}_{0.08}\text{S@SC/SCWF}$  rechargeable ZAB, with  $\text{Fe}_{0.92}\text{Co}_{0.08}\text{S@SC/SCWF}$



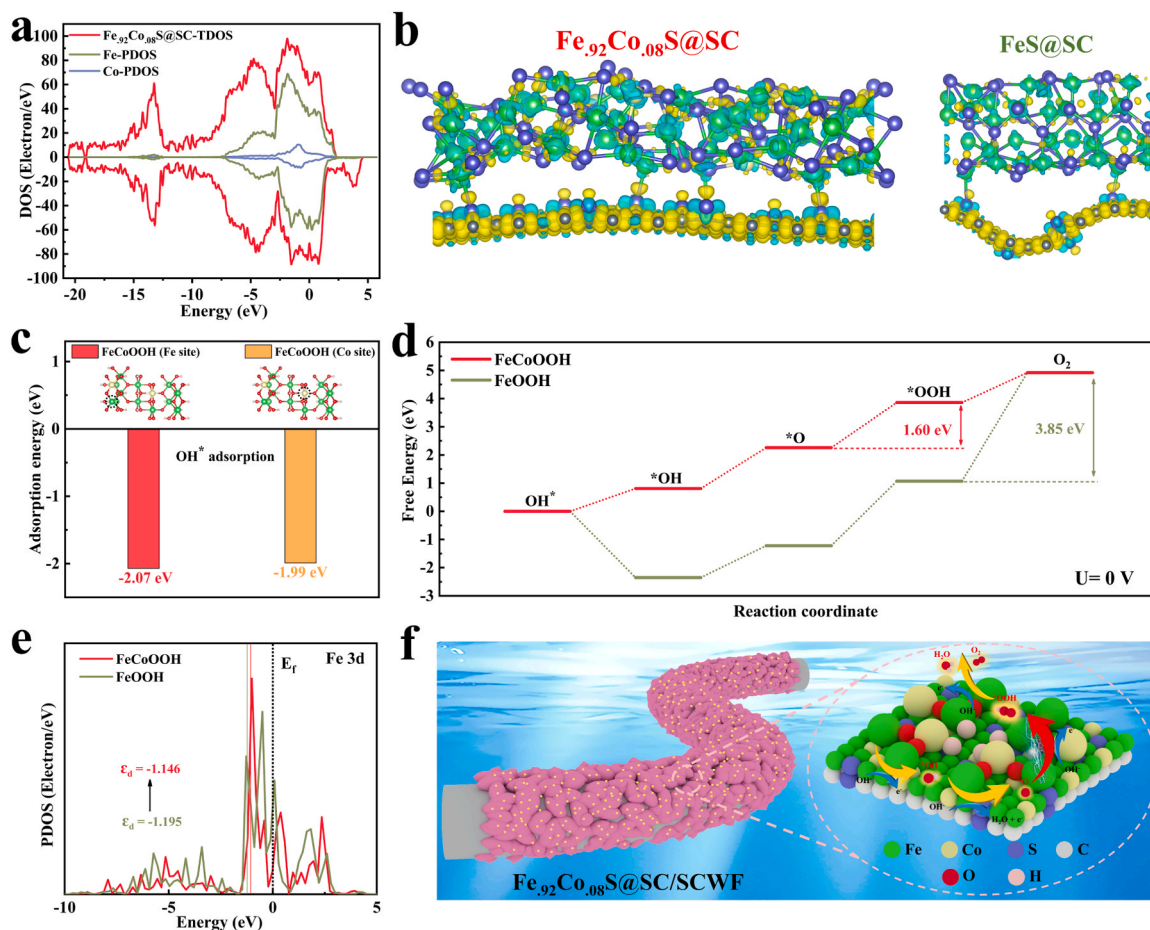


**Fig. 5.** (a) DOS of Fe<sub>92</sub>Co<sub>08</sub>S@SC, PDOS of Fe and Co; (b) Charge density difference of Fe<sub>92</sub>Co<sub>08</sub>S@SC and FeS@SC (yellow and blue colors denote the accumulation and depletion of electrons); (c) Comparison of OH\* adsorption energies of Fe site and Co site in FeCoOOH; (d) OER free-energy ladder plots of FeCoOOH and FeOOH at U = 0 V; (e) PDOS of Fe in FeCoOOH and FeOOH; (f) Mechanism analysis.

+ Pt/C as the air cathode and zinc plate as the anode (Fig. 6a), to explore its potential in practical application devices. Compared with RuO<sub>2</sub> + Pt/C, Fe<sub>92</sub>Co<sub>08</sub>S@SC/SCWF + Pt/C showed a slightly smaller voltage gap during charge and discharge, which was mainly due to the better OER activity of Fe<sub>92</sub>Co<sub>08</sub>S@SC/SCWF than RuO<sub>2</sub>. The charge-discharge polarization curve (Fig. 6b) revealed a lower charge-discharge potential for Fe<sub>92</sub>Co<sub>08</sub>S@SC/SCWF + Pt/C than RuO<sub>2</sub> + Pt/C. As shown in Fig. 6c, the power density of Fe<sub>92</sub>Co<sub>08</sub>S@SC/SCWF + Pt/C (177.86 mW cm<sup>-2</sup>) was higher than that of RuO<sub>2</sub> (172.6 mW cm<sup>-2</sup>) and is better than most reported ZAB performance (Fig. 6d and Table S4). As shown in Fig. 6e, the open-circuit voltage of a zinc-air cell loaded with Fe<sub>92</sub>Co<sub>08</sub>S@SC/SCWF + Pt/C was 1.42 V, which can successfully light up light emitting diodes (Fig. 6f). Fig. 6g also reveals that Fe<sub>92</sub>Co<sub>08</sub>S@SC/SCWF + Pt/C has a superior cycle stability, superior to that of RuO<sub>2</sub>. The above results confirmed that Fe<sub>92</sub>Co<sub>08</sub>S@SC/SCWF has more potential for practical application in ZAB than RuO<sub>2</sub>.

#### 4. Conclusion

We successfully encapsulated Fe<sub>92</sub>Co<sub>08</sub>S with bimetallic synergies within the S-doped carbon matrix and anchored them uniformly onto the SCWF substrate through synchronous carbonization and sulfurization. The synergistic catalysis of Fe and Co bimetallic in Fe<sub>92</sub>Co<sub>08</sub>S@SC greatly enhanced the catalytic performance against OER. Given the unique structural effect, the Fe<sub>92</sub>Co<sub>08</sub>S@SC/SCWF-supported electrocatalysts avoided the agglomeration of Fe<sub>92</sub>Co<sub>08</sub>S@SC, provided a large specific surface area for the reaction, and enhanced conductivity.

Driving the OER process at current densities of 50 and 100 mA cm<sup>-2</sup>, Fe<sub>92</sub>Co<sub>08</sub>S@SC/SCWF required overpotentials of 238 and 252 mV, respectively, and a Tafel slope of 35.89 mV dec<sup>-1</sup>. Moreover, 281 mV was required to achieve a high current density of 500 mA cm<sup>-2</sup>. Notably, the electrocatalyst showed excellent stability over 100 h with almost no attenuation of the catalytic activity (0.14%). As the air cathode catalyst of ZAB, which has broad application prospects, its power density reached 177.86 mW cm<sup>-2</sup>. DFT calculations confirm that the introduction of Co as a promoter into Fe<sub>92</sub>Co<sub>08</sub>S@SC increases the electron density of Fe, and accelerates the surface reconstruction of Fe<sub>92</sub>Co<sub>08</sub>S@SC to generate FeCoOOH with efficient OER catalytic performance. This work presented a design method for the production of effective OER electrocatalysts utilizing sustainable WF resources and provides insights into the synergistic mechanism of electrocatalysts containing bimetal.

#### CRediT authorship contribution statement

**Sha Chen:** Funding acquisition, Formal analysis. **Han Xu:** Writing – review & editing, Project administration, Funding acquisition, Formal analysis, Conceptualization. **Yu Liao:** Investigation. **Yuanyuan Liao:** Investigation. **Yan Qing:** Supervision, Funding acquisition. **Yiqiang Wu:** Supervision, Funding acquisition. **Bin Zhao:** Writing – original draft, Methodology, Investigation, Formal analysis, Data curation. **Wanjuan Zeng:** Investigation, Data curation. **Wenxi Zhang:** Investigation.



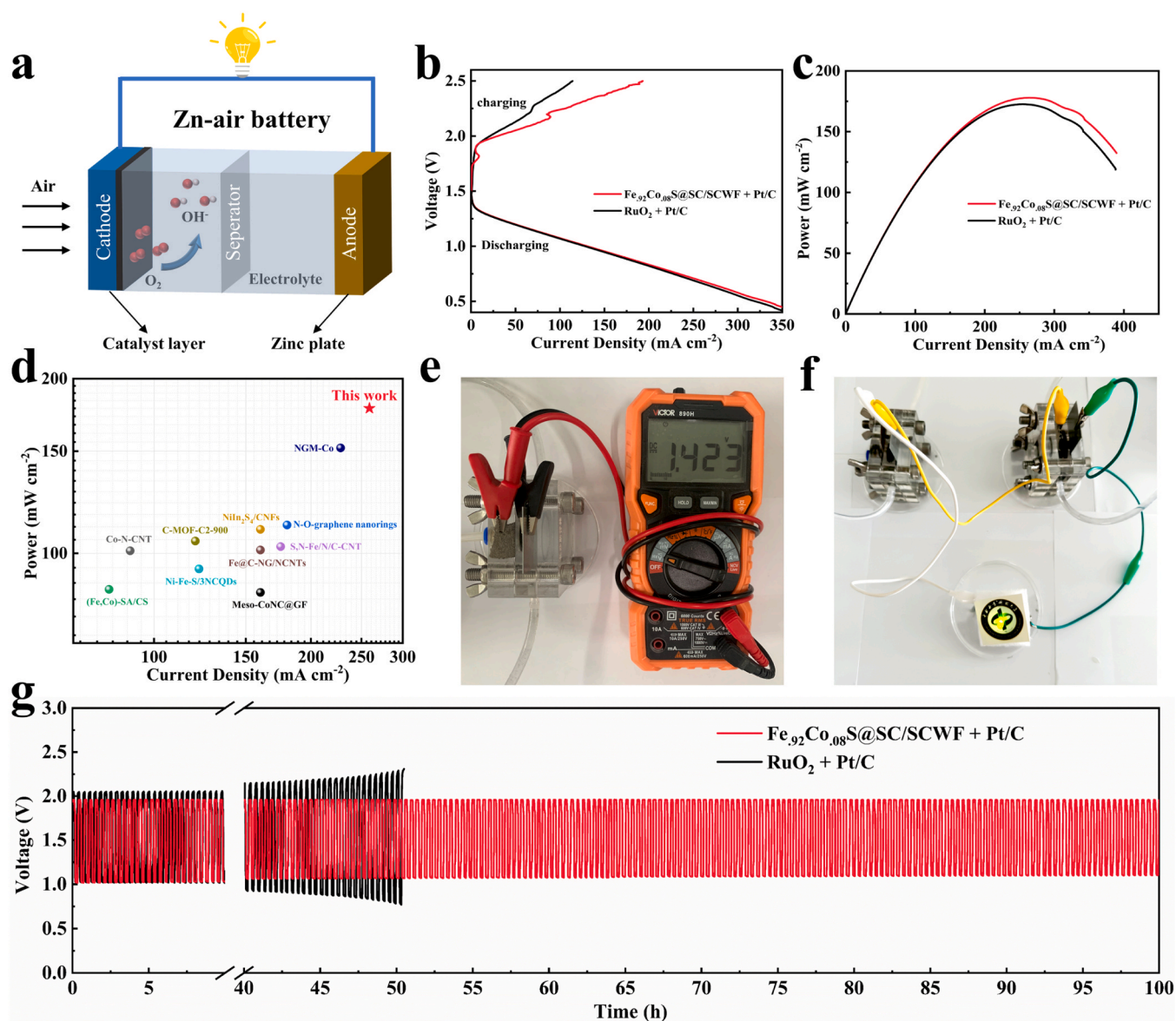


**Fig. 6.** (a) Schematic of ZAB. (b) Charge-discharge curves of ZAB loaded with  $\text{Fe}_{92}\text{Co}_{08}\text{S@SC/SCWF} + \text{Pt/C}$  and  $\text{RuO}_2 + \text{Pt/C}$ . (c) Power density curve. (d) Comparison with recently reported ZAB performance. (e) Open-circuit voltage of ZAB loaded with  $\text{Fe}_{92}\text{Co}_{08}\text{S@SC/SCWF} + \text{Pt/C}$  and (f) images of lit LED bulbs. (g) Constant current charge and discharge curve.

### Declaration of Competing Interest

The authors declare that they have no known competing financial interests or personal relationships that could have appeared to influence the work reported in this paper.

### Data availability

Data will be made available on request.

### Acknowledgements

This work was financially supported by National Natural Science Foundation of China (31890771 and 32271792), the Young Elite Scientists Sponsorship Program from National Forestry and Grassland Administration of China (2019132614), the Science and Technology Innovation Program of Hunan Province (2021RC3103 and 2022RC3054), and the Scientific Research Project of Hunan Provincial Education Department (21B0225 and 21C0143). The authors also thank

Shiyanjia Lab ([www.shiyanjia.com](http://www.shiyanjia.com)) for the support of TEM, XPS, and DFT analyses.

### Appendix A. Supporting information

Supplementary data associated with this article can be found in the online version at [doi:10.1016/j.apcatb.2024.123947](https://doi.org/10.1016/j.apcatb.2024.123947).

### References

- [1] Z.W. Seh, J. Kibsgaard, C.F. Dickens, I. Chorkendorff, J.K. Nørskov, T.F. Jaramillo, Combining theory and experiment in electrocatalysis: insights into materials design, *Science* 355 (2017) 4998.
- [2] X.F. Lu, L. Yu, X.W. Lou, Highly crystalline Ni-doped FeP/carbon hollow nanorods as all-pH efficient and durable hydrogen evolving electrocatalysts, *Sci. Adv.* 5 (2) (2019) 6009.
- [3] Y. Huang, S.L. Zhang, X.F. Lu, Z.P. Wu, D. Luan, X.W. Lou, Trimetallic spinel  $\text{NiCo}_2\text{xFe}_x\text{O}_4$  nanoboxes for highly efficient electrocatalytic oxygen evolution, *Angew. Chem. Int. Ed.* 60 (21) (2021) 11841–11846.
- [4] C.F. Li, J.W. Zhao, L.J. Xie, J.Q. Wu, Q. Ren, Y. Wang, G.R. Li, Surface-adsorbed carboxylate ligands on layered double hydroxides/metal-organic frameworks

- promote the electrocatalytic oxygen evolution reaction, *Angew. Chem. Int. Ed.* 60 (33) (2021) 18129–18137.
- [5] L. Tang, T. Fan, Z. Chen, J. Tian, H. Guo, M. Peng, F. Zuo, X. Fu, M. Li, Y. Bu, Y. Luo, J. Li, Y. Sun, Binary-dopant promoted lattice oxygen participation in OER on cobaltate electrocatalyst, *Chem. Eng. J.* 417 (2021) 129324.
  - [6] Z. Wang, J. Huang, L. Wang, Y. Liu, W. Liu, S. Zhao, Z.Q. Liu, Cation-tuning induced d-band center modulation on Co-based spinel oxide for oxygen reduction/evolution reaction, *Angew. Chem. Int. Ed.* 61 (16) (2022) 202114696.
  - [7] M. Song, X. Tao, Y. Wu, Y. Qing, C. Tian, H. Xu, X. Lu, Boosting oxygen evolution activity of NiFe layered double hydroxide through interface engineering assisted with naturally-hierarchical wood, *Chem. Eng. J.* 421 (2021) 129751.
  - [8] X.T. Wang, T. Ouyang, L. Wang, J.H. Zhong, T. Ma, Z.Q. Liu, Redox-inert Fe<sup>3+</sup> ions in octahedral sites of Co-Fe spinel oxides with enhanced oxygen catalytic activity for rechargeable zinc-air batteries, *Angew. Chem. Int. Ed.* 58 (38) (2019) 13291–13296.
  - [9] Y. Wu, X. Tao, Y. Qing, H. Xu, F. Yang, S. Luo, C. Tian, M. Liu, X. Lu, Cr-doped FeNi-P nanoparticles encapsulated into N-doped carbon nanotube as a robust bifunctional catalyst for efficient overall water splitting, *Adv. Mater.* 31 (15) (2019) 1900178.
  - [10] C.F. Li, L.J. Xie, J.W. Zhao, L.F. Gu, H.B. Tang, L. Zheng, G.R. Li, Interfacial Fe-O-Ni-O-Fe bonding regulates the active Ni sites of Ni-MOFs via iron doping and decorating with FeOOH for super-efficient oxygen evolution, *Angew. Chem. Int. Ed.* 61 (17) (2022) 202116934.
  - [11] H. Liao, X. Zhang, S. Niu, P. Tan, K. Chen, Y. Liu, G. Wang, M. Liu, J. Pan, Dynamic dissolution and re-adsorption of molybdate ion in iron incorporated nickel-molybdenum oxyhydroxide for promoting oxygen evolution reaction, *Appl. Catal. B: Environ.* 307 (2022) 121150.
  - [12] X. Ren, T. Wu, Y. Sun, Y. Li, G. Xian, X. Liu, C. Shen, J. Gracia, H.J. Gao, H. Yang, Z. J. Xu, Spin-polarized oxygen evolution reaction under magnetic field, *Nat. Commun.* 12 (2021) 2608.
  - [13] H. Liao, T. Luo, P. Tan, K. Chen, L. Lu, Y. Liu, M. Liu, J. Pan, Unveiling role of sulfate ion in nickel-iron (oxy) hydroxide with enhanced oxygen-evolving performance, *Adv. Funct. Mater.* 31 (2021) 2102772.
  - [14] Z.F. Huang, S. Xi, J. Song, S. Dou, X. Li, Y. Du, C. Diao, Z.J. Xu, X. Wang, Tuning of lattice oxygen reactivity and scaling relation to construct better oxygen evolution electrocatalyst, *Nat. Commun.* 12 (2021) 3992.
  - [15] H. Liao, G. Ni, P. Tan, K. Liu, X. Liu, H. Liu, K. Chen, X. Zheng, M. Liu, J. Pan, Oxyanion engineering suppressed iron segregation in nickel-iron catalysts toward stable water oxidation, *Adv. Mater.* 35 (2023) 2300347.
  - [16] H. Liao, G. Ni, P. Tan, Y. Liu, K. Chen, G. Wang, M. Liu, J. Pan, Borate narrowed band gap of nickel-iron layer double hydroxide to mediate rapid reconstruction kinetics for water oxidation, *Appl. Catal. B: Environ.* 317 (2022) 121713.
  - [17] J. Suntivich, K.J. May, H.A. Gasteiger, J.B. Goodenough, Y. Shao-Horn, A perovskite oxide optimized for oxygen evolution catalysis from molecular orbital principles, *Science* 334 (2011) 1383–1385.
  - [18] Z. Li, X. Zhang, Z. Zhang, P. Chen, Y. Zhang, X. Dong, Dual-metal hydroxide@oxide heterojunction catalyst constructed via corrosion engineering for large-current oxygen evolution reaction, *Appl. Catal. B: Environ.* 325 (2023) 122311.
  - [19] X. Tao, H. Xu, S. Luo, Y.Q. Wu, C.H. Tian, X.H. Lu, Y. Qing, Construction of N-doped carbon nanotube encapsulated active nanoparticles in hierarchically porous carbonized wood frameworks to boost the oxygen evolution reaction, *Appl. Catal. B: Environ.* 279 (2020) 119367.
  - [20] H. Xu, Z.X. Shi, Y.X. Tong, G.R. Li, Porous microrod arrays constructed by carbon-confined NiCo@NiCoO<sub>2</sub> core@shell nanoparticles as efficient electrocatalysts for oxygen evolution, *Adv. Mater.* 30 (21) (2018) 1705442.
  - [21] N. Zhang, Y. Hu, L. An, Q. Li, J. Yin, J. Li, R. Yang, M. Lu, S. Zhang, P. Xi, C.H. Yan, Surface activation and Ni-S stabilization in NiO/NiS<sub>2</sub> for efficient oxygen evolution reaction, *Angew. Chem. Int. Ed.* 61 (2022) 202207217.
  - [22] Z. Pei, X.F. Lu, H. Zhang, Y. Li, D. Luan, X.W.D. Lou, Highly efficient electrocatalytic oxygen evolution over atomically dispersed synergistic Ni/Co dual sites, *Angew. Chem. Int. Ed.* 61 (2022) 202207537.
  - [23] L. Yan, B. Xie, C. Yang, Y. Wang, J. Ning, Y. Zhong, Y. Hu, Engineering self-supported hydrophobic-aerophilic air cathode with CoS/Fe<sub>3</sub>S<sub>4</sub> nanoparticles embedded in S, N Co-doped carbon plate arrays for long-life rechargeable Zn-air batteries, *Adv. Energy Mater.* 13 (2023) 2204245.
  - [24] H.F. Wang, L. Chen, H. Pang, S. Kaskel, Q. Xu, MOF-derived electrocatalysts for oxygen reduction, oxygen evolution and hydrogen evolution reactions, *Chem. Soc. Rev.* 49 (2020) 1414–1448.
  - [25] G. Cai, W. Zhang, L. Jiao, S.H. Yu, H.L. Jiang, Template-directed growth of well-aligned MOF arrays and derived self-supporting electrodes for water splitting, *Chem* 2 (2017) 791–802.
  - [26] Z. Jiang, L. Zheng, C. Sheng, H. Xu, S. Chen, Y. Liao, Y. Qing, Y. Wu, Construction of NiS/Ni<sub>3</sub>S<sub>4</sub> heteronanorod arrays in graphitized carbonized wood frameworks as versatile catalysts for efficient urea-assisted water splitting, *J. Colloid Interface Sci.* 626 (2022) 848–857.
  - [27] J. Kang, F. Yang, C. Sheng, H. Xu, J. Wang, Y. Qing, Y. Wu, X. Lu, CoP nanoparticle confined in P, N Co-doped porous carbon anchored on P-doped carbonized wood fibers with tailored electronic structure for efficient urea electro-oxidation, *Small* 18 (2022) 2200950.
  - [28] T.N. Ye, L.B. Lv, X.H. Li, M. Xu, J.S. Chen, Strongly veined carbon nanoleaves as a highly efficient metal-free electrocatalyst, *Angew. Chem. Int. Ed.* 53 (2014) 6905–6909.
  - [29] T. Liu, Y.F. Guo, Y.M. Yan, F. Wang, C. Deng, D. Rooney, K.-N. Sun, CoO nanoparticles embedded in three-dimensional nitrogen/sulfur co-doped carbon nanofiber networks as a bifunctional catalyst for oxygen reduction/evolution reactions, *Carbon* 106 (2016) 84–92.
  - [30] C. Yang, Q. Wu, W. Xie, X. Zhang, A. Brozena, J. Zheng, M.N. Garaga, B.H. Ko, Y. Mao, S. He, Y. Gao, P. Wang, M. Tyagi, F. Jiao, R. Briber, P. Albertus, C. Wang, S. Greenbaum, Y.Y. Hu, A. Isogai, M. Winter, K. Xu, Y. Qi, L. Hu, Copper-coordinated cellulose ion conductors for solid-state batteries, *Nature* 598 (2021) 590–596.
  - [31] S. Zhang, R. Dong, M. Wang, W. Jia, Z. Lu, Synthesis mechanisms on waste poplar fiber lightweight biomass bricks, *J. Clean. Prod.* 246 (2020) 118981.
  - [32] J. Yu, W.-J. Li, G. Kao, C.Y. Xu, R. Chen, Q. Liu, J. Liu, H. Zhang, J. Wang, In-situ growth of CNTs encapsulating P-doped NiSe<sub>2</sub> nanoparticles on carbon framework as efficient bifunctional electrocatalyst for overall water splitting, *J. Energy Chem.* 60 (2021) 111–120.
  - [33] J. Wu, Q. Zhang, K. Shen, R. Zhao, W. Zhong, C. Yang, H. Xiang, X. Li, N. Yang, Modulating interband energy separation of boron-doped Fe<sub>7</sub>S<sub>6</sub>/FeS<sub>2</sub> electrocatalysts to boost alkaline hydrogen evolution reaction, *Adv. Funct. Mater.* 32 (2021) 2107802.
  - [34] P. Zhang, Y. Liu, T. Liang, E.H. Ang, X. Zhang, F. Ma, Z. Dai, Nitrogen-doped carbon wrapped Co-Mo<sub>2</sub>C dual Mott-Schottky nanosheets with large porosity for efficient water electrolysis, *Appl. Catal. B: Environ.* 284 (2021) 119738.
  - [35] W. Liu, J. Zhang, Z. Bai, G. Jiang, M. Li, K. Feng, L. Yang, Y. Ding, T. Yu, Z. Chen, A. Yu, Controllable urchin-like NiCo<sub>2</sub>S<sub>4</sub> microsphere synergized with sulfur-doped graphene as bifunctional catalyst for superior rechargeable Zn-air battery, *Adv. Funct. Mater.* 28 (2018) 1706675.
  - [36] Q. Zhou, S. Hou, Y. Cheng, R. Sun, W. Shen, R. Tian, J. Yang, H. Pang, L. Xu, K. Huang, Y. Tang, Interfacial engineering Co and MnO within N, S co-doped carbon hierarchical branched superstructures toward high-efficiency electrocatalytic oxygen reduction for robust Zn-air batteries, *Appl. Catal. B: Environ.* 295 (2021) 120281.
  - [37] B. Yin, X. Cao, A. Pan, Z. Luo, S. Dinesh, J. Lin, Y. Tang, S. Liang, G. Cao, Encapsulation of CoS<sub>x</sub> nanocrystals into N/S co-doped honeycomb-like 3D porous carbon for high-performance lithium storage, *Adv. Sci.* 5 (2018) 1800829.
  - [38] D. Guo, Z. Zeng, Z. Wan, Y. Li, B. Xi, C. Wang, A CoN-based OER electrocatalyst capable in neutral medium: atomic layer deposition as rational strategy for fabrication, *Adv. Funct. Mater.* 31 (2021) 2101324.
  - [39] Y. Yu, S. You, J. Du, Z. Xing, Y. Dai, H. Chen, Z. Cai, N. Ren, J. Zou, ZIF-67-derived CoO (tetrahedral Co<sup>2+</sup>)@nitrogen-doped porous carbon protected by oxygen vacancies-enriched SnO<sub>2</sub> as highly active catalyst for oxygen reduction and Pt co-catalyst for methanol oxidation, *Appl. Catal. B: Environ.* 259 (2019) 118043.
  - [40] J. Zhang, M. Zhang, Y. Zeng, J. Chen, L. Qiu, H. Zhou, C. Sun, Y. Yu, C. Zhu, Z. Zhu, Single Fe atom on hierarchically porous S, N-codoped nanocarbon derived from porphyrin enable boosted oxygen catalysis for rechargeable Zn-air batteries, *Small* 15 (2019) 1900307.
  - [41] Y. Zhang, Y. Wu, L. Wan, H. Ding, H. Li, X. Wang, W. Zhang, Hollow core-shell Co<sub>9</sub>S<sub>8</sub>@ZnIn<sub>2</sub>S<sub>4</sub>/CdS nanoreactor for efficient photothermal effect and CO<sub>2</sub> photoreduction, *Appl. Catal. B: Environ.* 311 (2022) 121255.
  - [42] C. Chen, M. Sun, F. Zhang, H. Li, M. Sun, P. Fang, T. Song, W. Chen, J. Dong, B. Rosen, P. Chen, B. Huang, Y. Li, Adjacent Fe site boosts electrocatalytic oxygen evolution at Co site in single-atom-catalyst through a dual-metal-site design, *Energy Environ. Sci.* 16 (2023) 1685–1696.
  - [43] J. Liu, X. Meng, J. Xie, B. Liu, B. Tang, R. Wang, C. Wang, P. Gu, Y. Song, S. Huo, J. Zou, Dual active sites engineering on sea urchin-like CoNiS hollow nanosphere for stabilizing oxygen electrocatalysis via a template-free vulcanization strategy, *Adv. Funct. Mater.* 33 (22) (2023) 2300579.
  - [44] Y. Liao, Y. Chen, L. Li, S. Luo, Y. Qing, C. Tian, H. Xu, J. Zhang, Y. Wu, Ultrafine homologous Ni<sub>2</sub>P-Co<sub>2</sub>P heterostructures via space-confined topological transformation for superior urea electrolysis, *Adv. Funct. Mater.* (2023) 2303300.
  - [45] D. Guo, X. Li, Y. Jiao, H. Yan, A. Wu, G. Yang, Y. Wang, C. Tian, H. Fu, A dual-active Co-CoO heterojunction coupled with Ti<sub>3</sub>C<sub>2</sub>-MXene for highly-performance overall water splitting, *Nano Res.* 15 (2021) 238–247.
  - [46] Z. Wang, L. Xu, F. Huang, L. Qu, J. Li, K.A. Owusu, Z. Liu, Z. Lin, B. Xiang, X. Liu, K. Zhao, X. Liao, W. Yang, Y.B. Cheng, L. Mai, Copper-nickel nitride nanosheets as efficient bifunctional catalysts for hydrazine-assisted electrolytic hydrogen production, *Adv. Energy Mater.* 9 (2019) 1900390.
  - [47] A. Wang, X. Zhang, S. Gao, C. Zhao, S. Kuang, S. Lu, J. Niu, G. Wang, W. Li, D. Chen, H. Zhang, X. Zhou, S. Zhang, B. Zhang, W. Wang, Fast-charging Zn-air batteries with long lifetime enabled by reconstructed amorphous multi-metallic sulfide, *Adv. Mater.* 34 (2022) 2204247.
  - [48] L. Tan, J. Yu, C. Wang, H. Wang, X. Liu, H. Gao, L. Xin, D. Liu, W. Hou, T. Zhan, Partial sulfidation strategy to NiFe-LDH@FeNi<sub>2</sub>S<sub>4</sub> heterostructure enable high-performance water/seawater oxidation, *Adv. Funct. Mater.* 32 (2022) 2200951.
  - [49] G. Genchev, A. Erbe, Raman spectroscopy of mackinawite FeS in anodic iron sulfide corrosion products, *J. Electrochem. Soc.* 163 (2016) C333.
  - [50] M. Cai, Q. Zhu, X. Wang, Z. Shao, L. Yao, H. Zeng, X. Wu, J. Chen, K. Huang, S. Feng, Formation and stabilization of NiOOH by introducing α-FeOOH in LDH: composite electrocatalyst for oxygen evolution and urea oxidation reactions, *Adv. Mater.* 35 (2023) 2209338.
  - [51] T.X. Nguyen, Y.H. Su, C.C. Lin, J.M. Ting, Self-reconstruction of sulfate-containing high entropy sulfide for exceptionally high-performance oxygen evolution reaction electrocatalyst, *Adv. Funct. Mater.* 31 (2021) 2106229.
  - [52] Y. Gao, S. Qian, H. Wang, W. Yuan, Y. Fan, N. Cheng, H. Xue, T. Jiang, J. Tian, Boron-doping on the surface mediated low-valence Co centers in cobalt phosphide for improved electrocatalytic hydrogen evolution, *Appl. Catal. B: Environ.* 320 (2023) 122014.
  - [53] W.H. Lee, M.H. Han, Y.J. Ko, B.K. Min, K.H. Chae, H.S. Oh, Electrode reconstruction strategy for oxygen evolution reaction: maintaining Fe-CoOOH phase with intermediate-spin state during electrolysis, *Nat. Commun.* 13 (2022) 605.

- [54] C. Yang, W. Zhong, K. Shen, Q. Zhang, R. Zhao, H. Xiang, J. Wu, X. Li, N. Yang, Electrochemically reconstructed Cu-FeOOH/Fe<sub>3</sub>O<sub>4</sub> catalyst for efficient hydrogen evolution in alkaline media, *Adv. Energy Mater.* 12 (2022) 2200077.
- [55] J. Zhang, G. Chen, Q. Liu, C. Fan, D. Sun, Y. Tang, H. Sun, X. Feng, Competitive adsorption: reducing the poisoning effect of adsorbed hydroxyl on Ru single-atom site with SnO<sub>2</sub> for efficient hydrogen evolution, *Angew. Chem. Int. Ed.* 61 (2022) 202209486.
- [56] C. Fu, X. Qi, L. Zhao, T. Yang, Q. Xue, Z. Zhu, P. Xiong, J. Jiang, X. An, H. Chen, J. S. Chen, A. Cabot, R. Wu, Synergistic cooperation between atomically dispersed Zn and Fe on porous nitrogen-doped carbon for boosting oxygen reduction reaction, *Appl. Catal. B: Environ.* 335 (2023) 122875.
- [57] J.N. Liu, C.X. Zhao, J. Wang, D. Ren, B.Q. Li, Q. Zhang, A brief history of zinc-air batteries: 140 years of epic adventures, *Energy Environ. Sci.* 15 (2022) 4542–4553.